

Check for updates





Numerical Modeling of Photothermal Self-Excited Composite Oscillators

Zixiao Liu¹ | Ryan R. Rusch¹ | Zheng Wu¹ | Chi Chen¹ | Pengju Shi¹ | Hao Qiu² | Ximin He¹

¹Department of Materials Science and Engineering, University of California, Los Angeles, Los Angeles, California, USA | ²University of California, Berkeley, Berkeley, California, USA

Correspondence: Ximin He (ximinhe@ucla.edu)

Received: 3 September 2025 | Revised: 22 October 2025 | Accepted: 28 October 2025

Funding: American Chemical Society, Grant/Award Number: 66747-ND7; Johnson & Johnson, Grant/Award Number: 20231448; Inventor Fellow, Grant/Award Number: 12072; National Institutes of Health, Grant/Award Number: R01DK132319; Moore Foundation, Grant/Award Number: 12072; Semiconductor Research Corporation, Grant/Award Number: 2023-JU3136; Office of Naval Research, Grant/Award Numbers: N000142412187 N000142212595

Keywords: composite structure | liquid crystal elastomer | numerical simulation | self-excited oscillation

ABSTRACT

Autonomous motion, such as self-excited oscillation, emerges from the intricate interaction between structural deformation and external stimulation. By carefully engineering this interaction, diverse modes of locomotion have been achieved without the need for real-time human control or external intervention. However, quantitatively capturing and modeling such behavior inevitably require solving a set of highly coupled equations across multiple physical fields. In this study, we develop a numerical framework for simulating photothermal self-excited composite oscillators, which couples the light-heat conversion, the heat transfer within the composite, and thermal strain-induced large deformation. We systematically study the influence of various operating conditions and material properties on oscillation and establish the criteria and conditions for the onset of self-excited oscillation. This study aims to provide design guidelines for future autonomous actuators and robotic systems.

1 | Introduction

Self-excited oscillation is a periodic motion initiated and sustained by a constant, nonoscillatory energy input [1], without real-time human control, preprogrammed input waveforms, or external frequency tuning. Owing to its autonomous operation, self-regulation, and minimal control requirements, self-excited oscillators have garnered increasing attention for sensing (e.g., oscillatory flow meters [2]), energy harvesting (e.g., flow-induced vibrations of triboelectric harvesters [3]), and actuation (e.g., self-oscillating actuators [4]).

A variety of stimuli-responsive materials have been used to build self-excited oscillators, including hydrogels, liquid crystal polymers, and shape-memory polymers, enabling diverse modes of motion, such as walking, swimming, and flying [4–7].

Photothermal liquid crystal elastomers (LCEs) are particularly promising due to their large actuation strain and fast response speed. Unlike hydrogel, whose reconfiguration relies on solvent absorption/desorption [6] or on chemical reactions (e.g., Belousov–Zhabotinsky reactions [8]) and is therefore limited by slow diffusion or reaction kinetics, photothermal LCEs undergo a rapid nematic-to-isotropic transition at elevated temperature, producing large, fast, and highly directional contraction. LCE-based self-excited oscillators exhibit larger oscillation amplitude and frequency in air, without relying on the solvent environment.

Unlike forced vibration—where excitation is prescribed independently of the system state—self-excited oscillation arises from a complex interplay between the system's internal state and the environmental stimulus: the stimulus modifies the system state, and the state evolution in turn alters the effective input. Various

This is an open access article under the terms of the Creative Commons Attribution License, which permits use, distribution and reproduction in any medium, provided the original work is properly cited.

© 2025 The Author(s). Advanced Robotics Research published by Wiley-VCH GmbH.

forms of LCE self-excited oscillation have been proposed, including vibrating fibers [9–11] and beams [12], rotation motion (LCE pendula and rotators) [13-17], ball bouncing [18], and balloon jump [19, 20]. For example, when a segment of photochemical LCE fiber is illuminated by constant light, it contracts and leaves the illuminated zone. Upon exiting, it cools and recovers, then reenters the zone. Its actuation strain and cis-state population (system state) are set by local light intensity (environmental stimulus), while the intensity depends on the fiber's deformation. In this study, we focus on the self-excited oscillation of a LCE beam (Figure 1a). Consider a horizontal cantilever irradiated by a laser aligned with its midplane. When the beam bends upward under an initial velocity, the lower surface faces the incident light and heats, contracting more than the upper surface that faces away from the light. The resulting through-thickness thermal strain gradient generates a thermal bending moment that drives the beam downward. By inertia, the beam overshoots the horizontal position, exposing the upper surface to the light and reversing the process. This alternating light exposure establishes feedback between structural deformation and effective photothermal input that sustains oscillation.

Analytical modeling of this photothermomechanical system is challenging due to strong nonlinearities and multiphysics coupling. It is required to establish the projection from incident light to effective heat input as a function of instantaneous beam bending angle, capture transient heat transfer, and translate the temperature field into thermal strain, stress, and bending moment. Beam bending modulates the heat input to the system, while the modulated input alters the bending—yielding a set of tightly coupled partial differential equations (structural dynamics and heat transfer) with moving boundaries and spatiotemporally varying

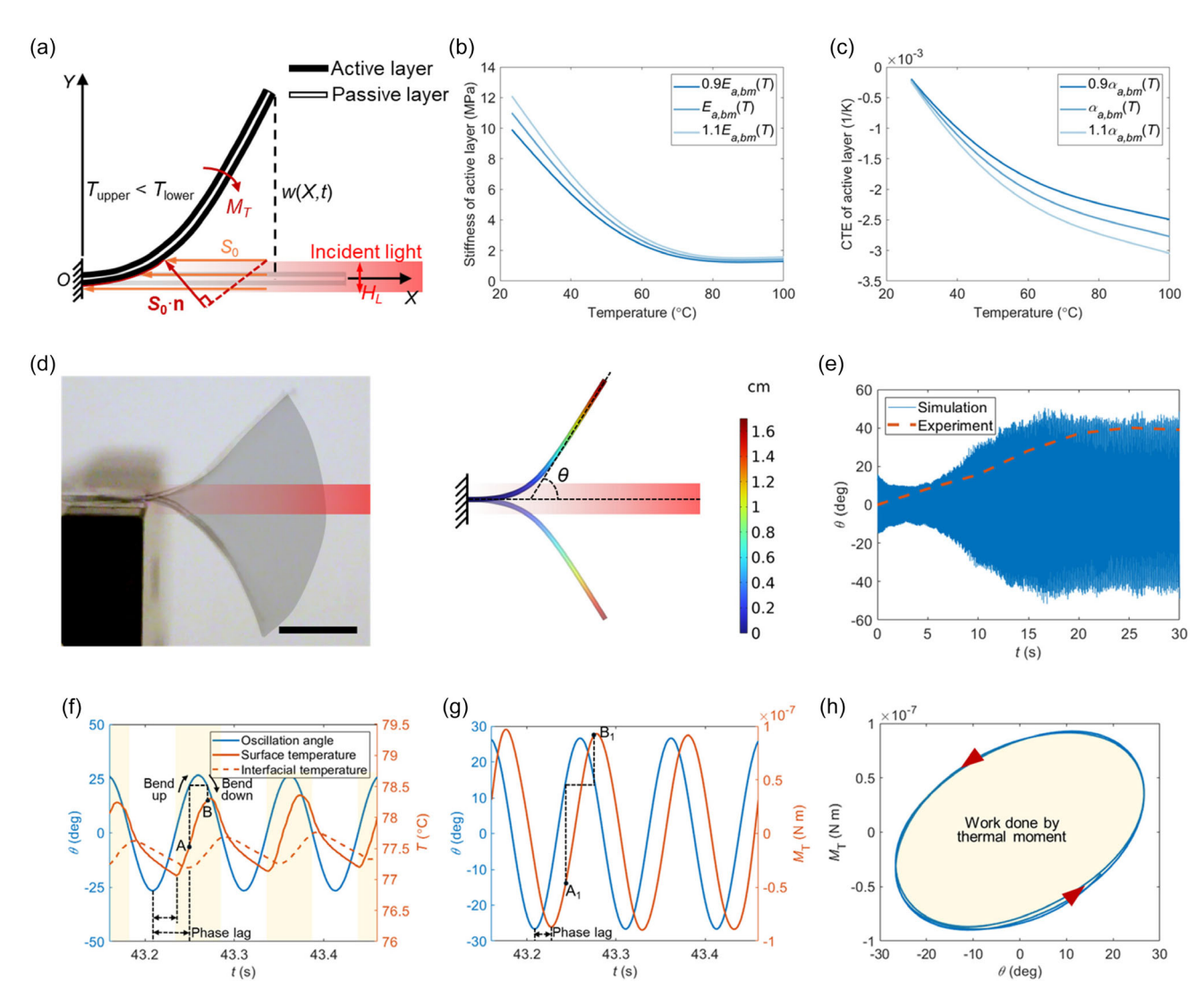


FIGURE 1 | Self-excited oscillation of the benchmark photothermal LCE/PDMS/LCE composite beam in experiments and simulations. (a) Schematic illustration of the self-excited oscillation mechanism. (b–c) Experimentally measured temperature-dependent stiffness $E_a(T)$ (b) and coefficient of thermal expansion $\alpha_a(T)$ (c) of the active layer. (d) Superimposed images of the oscillating beam in experiments (left, scale bar: 1 cm) and simulations (right; color map indicates displacement magnitude), showing comparable oscillation amplitudes and beam shapes. (e) Time evolution of the oscillation angle; the pink dashed line denotes the envelope of the experimental curve, while the blue solid line represents the simulated oscillation. (f–h) Phase lag and photothermal work at the illuminated region (X/L = 0.3) after steady oscillation. (f) Oscillation angle θ (blue), bottom-surface temperature (solid orange), and lower interfacial temperature (solid orange) versus time; labels A and B mark the same angle but different temperatures during bend-up and bend-down. (g) Phase lag between θ (blue) and thermal moment M_T (orange). (h) $M_T-\theta$ loop; enclosed area is the work done by M_T per cycle.

2 of 7 Advanced Robotics Research, 2025

boundary conditions. Additional material nonlinearities arise because some key LCE properties, including stiffness E(T) and the coefficient of thermal expansion (CTE) $\alpha(T)$, are temperature-dependent (Figure 1b,c). In this study, we focus on a trilayer active/passive/active architecture—previously found to outperform a unimorph active oscillator [4]—which further complicates analytical treatment due to heterogeneous photothermomechanical responses across layers. Simplified models, such as spring-mass-damper analogs [21] or prescribed temperature fields (an open-loop approximation), can offer qualitative insights but typically cannot capture the fully coupled dynamics and feedback governing the system.

Numerical simulation, therefore, provides a more tractable and robust route to capture the dynamics of photothermal self-excited composite oscillators. In this study, we develop a numerical framework that fully resolves the photothermomechanical coupling to elucidate the mechanism sustaining oscillation. We establish the criteria and conditions for the onset of self-excited oscillation across various material properties and operating conditions. This work aims to provide design guidelines for future autonomous actuators and robotic systems.

2 | Model and Formulation

Consider a composite cantilever beam consisting of a photothermally passive layer (polydimethylsiloxane; PDMS) sandwiched between two active layers (photothermal LCEs), irradiated by a constant near-infrared (NIR) laser with fixed intensity and incident direction. The absorbed NIR light can efficiently convert into heat, inducing nematic-to-isotropic transitions and thermal contraction of the LCE. Rather than explicitly modeling the molecular-scale reconfiguration of LCE mesogens, we characterize the resulting macroscopic deformation using an effective coefficient of thermal expansion $\alpha(T)$, which relates the thermal strain $(\varepsilon_{\rm th})$ to the temperature change $(T-T_0)$ as

$$\varepsilon_{\rm th} = \alpha(T)(T - T_0) \tag{1}$$

Here, $T_0 = 293.15~\rm K$ is the reference temperature at which no thermal strain is present. Because the photothermal agent exhibits a high NIR absorption coefficient, the optical penetration depth is on the order of micrometers—negligible compared to the >100- μ m thickness of our LCE layer. Therefore, we treat photothermal heating as a surface heat flux, neglecting light propagation within the LCE, and focus on the heat transfer, which is governed by

$$\rho_i C_{p,i} \frac{\partial T}{\partial t} + \nabla \cdot (-k_i \nabla T) = 0$$
 (2)

where index i = active and passive layers, ρ is the mass density, C_p is the specific heat capacity, and k is the thermal conductivity. The boundary heat flux applied to the upper and lower surfaces alternates with the oscillation and can be expressed as

$$q_{ir} = \eta S_0 \cdot \max[0, n_x(X, t)], \text{ at}|w(X, t)| < 0.5H_L$$
 (3)

where η is the photothermal conversion efficiency of LCE, n_x is the horizontal component of the outward unit normal of the deformed surface, and $H_{\rm L}$ is the height of the light spot. Segments of the beam outside the light spot do not receive light irradiation. The heat input increases with the beam's bending angle. Heat loss to the surroundings is modeled as $q_{\rm loss} = -\lambda (T-T_0)$, where λ is the convection coefficient. The heat transfer process and the spatiotemporal temperature profiles are simulated using the Heat Transfer in Solids interface in COMSOL Multiphysics.

The mechanical quantities, including stress, strain, and displacement, are solved using finite deformation theory without any structural assumptions (e.g., section shape and orientation, shear stress and deformation, and displacement field), implemented via the Solid Mechanics interface in COMSOL. Geometric nonlinearity is included to avoid nonphysical deformation (Supplemental Note 1). Compared to classical beam models (e.g., Euler-Bernoulli and Timoshenko beam), our approach is more appropriate for capturing large-amplitude oscillations. Both LCE and PDMS are treated with linear stress-strain relations but with temperature-dependent E(T) and $\alpha(T)$. Because the viscous effects are negligible compared to elasticity in elastomers, the loss modulus is omitted. An initial velocity is given to break the initial configurational symmetry of the system. In experiments, we trigger the initial oscillation by manually tapping the beam's free end. To mimic this, we apply a prescribed displacement at the free end of the beam in simulations as $w(t) = 0.02 \cdot \sin(8\pi t)$ for t = 0 - 2.5 s. During this triggering stage, the beam is under irradiation. Air damping is assumed to be proportional to structural velocity. The mechanical and the thermal fields are coupled through Equation (1), implemented via the Thermal Expansion interface in COMSOL.

For numerical implementation, the displacement field is discretized using quadratic Lagrange elements, and the temperature field using linear elements. Free Triangular meshes are employed, with the mesh size determined based on the thermal diffusivity $k/(\rho C_{\rm p})$ and the timestep of simulations. Standard mesh convergence tests were conducted by halving the element size to see if consistent results could be obtained. A time-dependent study is conducted in COMSOL.

3 | Results and Discussion

In our previous experimental study [4], we identified a benchmark photothermal LCE-based composite oscillator that achieves an optimal kinetic power density through careful tuning of its geometric, mechanical, and thermomechanical properties. The benchmark system is defined by the following parameters: beam length L=2.5 cm, width b=2.5 mm, thickness of the active LCE layer $h_{\rm a}=140~\mu{\rm m}$, and thickness of the passive PDMS layer $h_{\rm p}=320~\mu{\rm m}$. The temperature-dependent stiffness E(T) and coefficient of thermal expansion $\alpha(T)$ of the LCE were experimentally determined via dynamic mechanical analysis (Figure 1b,c). The PDMS layer was modeled as a linear elastic material with a nearly constant stiffness of 750 kPa and negligible thermal responsiveness ($\alpha_{\rm p}=0$). The mass density of the beam was set to $1100~\rm kg~m^{-3}$. To validate the simulation framework described

Advanced Robotics Research, 2025 3 of 7

in Section 2, we first reproduced this benchmark configuration in numerical simulations. As shown in Figure 1d, the simulated system successfully captured the key features of the experimentally observed self-excited oscillatory behavior, including the maximum oscillation angle and the beam deformation profile. In experiments, the beam reached steady-state oscillation after \approx 20 s, achieving a peak oscillation angle of θ = 42.2°. In simulation, the system reached steady oscillation at 16.9 s with a peak angle of $\theta = 48.1^{\circ}$ (Figure 1e). Additionally, the simulated oscillation frequency f and kinetic power density P (Figure S1) are in good agreement with the experimental measurements. The energy conversion efficiency from light input to mechanical output is 0.31% (Supplemental Note 2). These results confirm that our simulation framework accurately reproduces the experimentally observed photothermal self-excited oscillations, validating its capacity to predict oscillation performance.

3.1 | Oscillation Mechanism

First, structural inertia and overshoot are critical for the onset of oscillation. Sufficient inertia allows the beam to carry kinetic energy past the equilibrium position to overshoot, which is essential because the periodic alternation of irradiation on the beam's top and bottom surfaces reverses the sign of the thermal bending moment to sustain oscillation. To isolate this effect, we performed additional quasistatic simulations by neglecting inertia in our benchmark system while keeping geometry, material parameters, and simulation conditions unchanged. After the triggering stage (0-2.5 s in Figure S3), the motion rapidly decays to $\theta = 0^{\circ}$ (blue curve in Figure S3). This inertia-free response can also be interpreted as light tracking. We tilted the incident light relative to the beam by an angle (10°). Without inertia, the beam settles into a tilted equilibrium that aligns with the incident light (red curve in Figure S3), akin to phototropism-like tracking reported for photothermal hydrogels with slow diffusion and deformation, whose mild dynamics are well approximated as quasistatic motion [22].

After the benchmark oscillator reached steady oscillation, we tracked the bending angle θ and the local temperature at the illuminated region (X/L = 0.3). A clear phase lag appears between θ (blue curve in Figure 1f) and the bottom-surface temperature (solid orange curve). When the beam bends upward from the horizontal equilibrium, the bottom surface is exposed to the laser and heats. Even after the peak angle is reached and the beam begins to bend downward (black arrows in Figure 1f), the bottom surface still faces the incident light and continues absorbing heat unit heating and dissipation balance. As a result, the temperature at the same position (same θ) differs between the bend-up and bend-down stages (points A and B in Figure 1f), evidencing the phase lag between oscillation angle θ and temperature T. We also monitored the interior temperature at the lower LCE/PDMS interface (dashed orange curve in Figure 1f). Its phase lag relative to θ is further amplified because heat diffusion from the surface to the interior takes additional time.

We then calculated the cross-sectional thermal bending moment M_T at the illuminated area (X/L = 0.3) according to Equation (4).

$$M_{\rm T} = b \int_{-h/2}^{h/2} E(T)\alpha(T)\Delta T(Y, t) \cdot Y dY \tag{4}$$

where h is the total thickness, Y is the through-thickness coordinate, and $\Delta T(Y,t) = T(Y,t) - T_0$ is the temperature rise relative to the thermal-strain reference temperature T_0 . The lag between θ and T translates into a corresponding lag between θ and M_T (Figure 1g) and produces a hysteresis loop in the M_T - θ plane (Figure 1h). The loop area equals the work done by the thermal moment per cycle. Self-excited oscillation persists when the work balances (steady oscillation) or exceeds the damping losses (flutter; unstable self-excited oscillation [1, 23]); otherwise, the motion decays.

3.2 | Operating Conditions

We next examined how operating conditions, including light intensity, convective cooling, beam-light misalignment, and ambient temperature, govern the feedback between structural response and environmental stimulus and thereby set the motion characteristics. Increasing the light intensity S_0 raises the absorbed irradiance $S = \eta S_0$ (where η is the LCE photothermal conversion efficiency) and thus the effective heat input $(S \cdot n)$. Reducing S from 20000 to $18750 \,\mathrm{W \cdot m}^{-2}$ lowers the oscillation amplitude θ . At $S = 18750 \text{ W} \cdot \text{m}^{-2}$, the motion damps out (Figure 2a). Although a phase lag between θ and M_T remains (Figure 2b), the $M_{\rm T}$ - θ loop area shrinks over time (Figure 2c), indicating diminishing thermal work per cycle that no longer compensates for energy dissipation. The laser spot size matters similarly: at fixed $S = 20000 \,\mathrm{W \cdot m^{-2}}$, enlarging the laser spot $H_{\rm L}$ increases the energy delivered per unit time, strengthening the feedback. Compared with a small spot ($H_{\rm L} = 4\,{\rm mm}$; blue curve in Figure S4), a large spot yields faster heating, greater thermal accumulation, and a rapid growth of oscillation amplitude θ $(H_L = 35 \text{ mm}; \text{ red curve in Figure S4})$. At $S = 20000 \text{ W} \cdot \text{m}^{-2}$, the minimum spot size $H_{\rm L}$ required for the onset of self-sustained oscillation is 3.25 mm (Figure S5a). State diagrams in the (S, H_L) plane and the (H_L, L) plane are also provided in Figure S5.

As a countereffect of thermal input, convective cooling dissipates heat from the system. We varied the convective heat transfer coefficient λ from 25 to 55 W·m $^{-2}$ ·K $^{-1}$ in Newton's law of cooling for convective boundaries $(q_{\rm loss}=-\lambda(T-T_0)$ on all oscillator boundaries). For a fixed light intensity and spot size, increasing λ reduces the oscillation amplitude θ ; when $\lambda \geq 55~{\rm W\cdot m}^{-2}\cdot{\rm K}^{-1}$, oscillation damps out (Figure S6). Because the onset of sustained oscillation depends on the balance and competition between the irradiance and cooling, we constructed a state diagram in (S,λ) space (Figure 2d) with a threshold curve separating sustained and damped regimes.

We then introduced a relative angle between the beam axis and the incident light (Figure 2e). The effective heat input to the system is the projection of the light vector \mathbf{S} onto the normal \mathbf{n} of the beam surface, $S_n = \mathbf{S} \cdot \mathbf{n}$. A surface segment is considered to be irradiated only if (i) it faces the light ($S_n < 0$, i.e., the \mathbf{S} and outward normal \mathbf{n} point in opposite directions) and (ii) it lies within the laser spot (distance d from the segment to the laser

4 of 7 Advanced Robotics Research, 2025

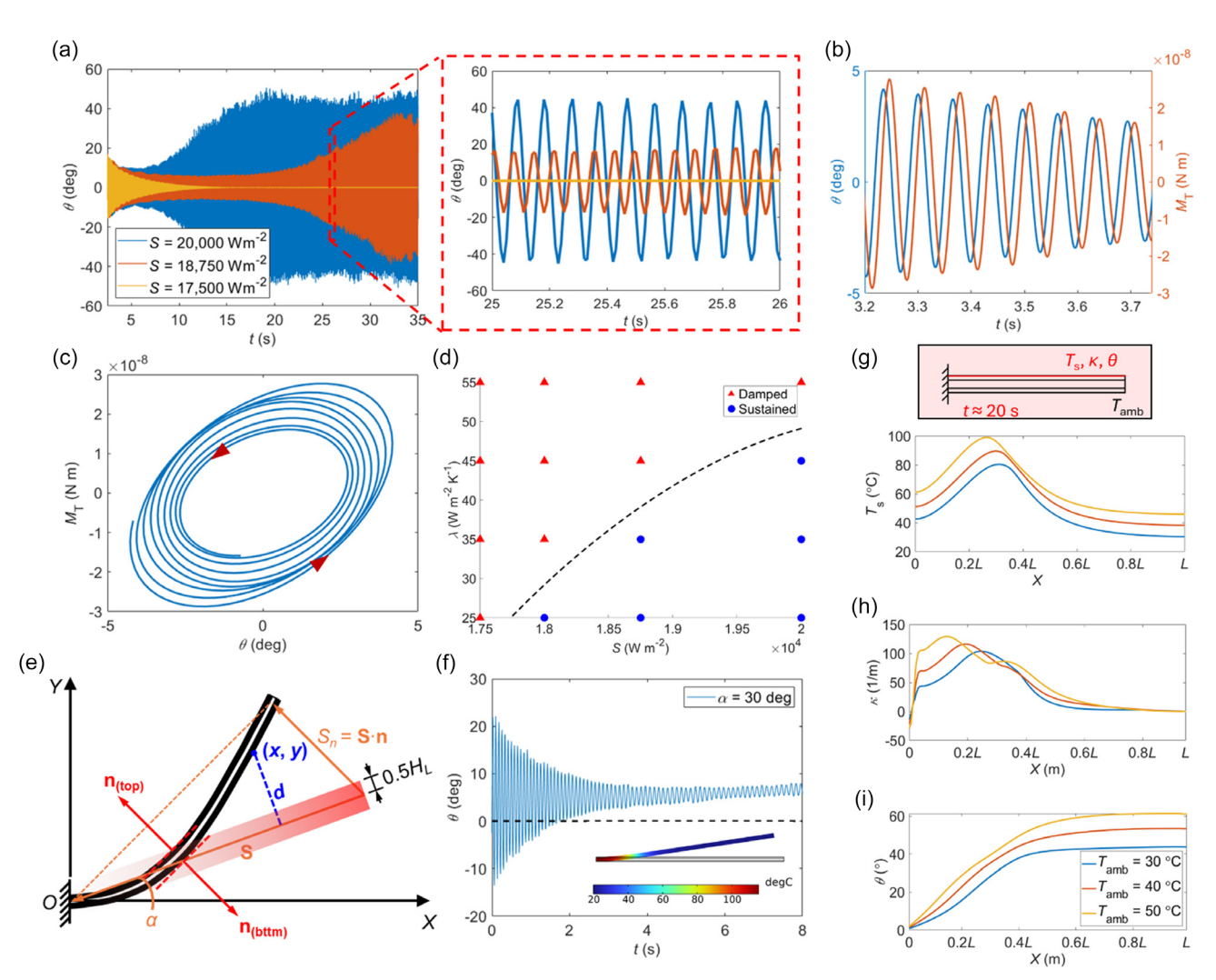


FIGURE 2 | Effect of operating conditions on oscillation. (a) Time histories of θ at S = 20000 (blue), 18750 (orange), and 17500 (yellow) W·m⁻² at $\lambda = 35 \text{ W·m}^{-2} \cdot \text{K}^{-1}$. Right zoom of t = 25-26 s. (b) Phase lag between θ (blue) and M_{T} (orange) at the illuminated region (X/L = 0.2 and Y/h = -1) for $S = 10000 \text{ W·m}^{-2}$. (c). $M_{\text{T}} - \theta$ loops showing decreasing work done by M_{T} per cycle as the motion damps. (d) $S - \lambda$ state diagram of self-sustained oscillation (blue dots) versus damped motion (red triangles); dashed curve indicates the approximate onset threshold. (e) A photothermal-responsive oscillator illuminated by a tilted laser beam. (f) Oscillation corresponding to a tilt angle of 30°. Insets: beam morphology and temperature at t = 20 s. (g-i) Effect of ambient temperature T_{amb} on surface temperature T_{g} (g), curvature κ (h), and bending angle θ (i).

centerline is less than $d < 0.5~H_{\rm L}$). Tilting establishes a stressed equilibrium configuration about which the oscillation is symmetric. The elastic stress associated with this tilted equilibrium tends to restore the beam toward its elastic stress-free (horizontal) configuration. As a result, part of the photothermal input is consumed in counteracting this elastic restoring stress rather than sustaining oscillation. Therefore, as the tilt angle increases, the oscillation amplitude decreases and eventually transitions to nonoscillating state (Figure 2f). The minimum tilt angle required for the onset of self-sustained oscillation is about 10– 15° (Figure S7).

Finally, we examined the effect of ambient temperature. Convection on all boundaries was modeled as $q = -\lambda (T_s - T_{amb})$, where T_s is the surface temperature. We varied the ambient temperature T_{amb} from 30 to 50 °C, and initialized the beam at 20 °C, mimicking transferring a cantilever from room temperature into an oven at T_{amb} , immediately turning on the laser (without waiting for the beam to reach thermal and mechanical equilibrium), and triggering oscillation. When $T_s < T_{amb}$, the environment

provides distributed heating over the entire beam; when $T_{\rm s} > T_{\rm amb}$, a higher $T_{\rm amb}$ reduces its temperature difference with $T_{\rm s}$ and thus net heat loss. Because the ambient acts over the entire beam rather than only the illuminated region, the overall temperature field rises with $T_{\rm amb}$ (Figure 2g), increasing the thermal-strain mismatch with the passive layer and thereby the curvature κ (Figure 2h) and bending angle θ (Figure 2i). Meanwhile, Larger θ in turn increases the projection of irradiance on the surface normal, further boosting heating and reinforcing the positive feedback. Collectively, the higher overall temperature, larger curvature, and feedback between bending and heating yield larger oscillation amplitude at higher $T_{\rm amb}$.

3.3 | Influence of Material Properties

Guided by the mechanism discussed above, we sought to increase the work done by the thermal moment $M_{\rm T}$ to enhance oscillation performance. From Equation (4), $M_{\rm T}$ scales with material

Advanced Robotics Research, 2025 5 of 7

stiffness E(T) and coefficient of thermal expansion $\alpha(T)$. We first scaled the benchmark stiffness [denoted as $E_{\rm a,bm}(T)$] by factors of 0.9 and 1.1 (Figure 3a) and quantified the impact on oscillation characteristics. As $E_{\rm a}$ increases, $M_{\rm T}$ grows and the oscillation amplitude θ increases. Consistent with beam dynamics, the oscillation frequency f also rises with stiffness. Then, we scaled the benchmark CTE $\alpha_{\rm a,bm}(T)$ by 0.9 and 1.1 (Figure 3b). Making $\alpha_{\rm a}(T)$ more negative increases θ , because a given temperature rise produces a larger contraction and therefore a larger thermal moment. This boosts beam deformation and oscillation amplitude. Practically, however, an excessively negative CTE can create a larger thermal-strain mismatch with the passive layer, risking interfacial delamination or failure.

A passive layer with $\alpha_p = 0$ does not contribute to thermal strain; increasing its stiffness only raises bending rigidity, reducing θ (Figure 3c). Although experiments primarily used thermally non-responsive middle layer [4, 5, 7], we explored the influence of middle layer CTE in simulations (Figure 3d). Varying α_p from -9×10^{-4} to $+9 \times 10^{-4}$ K⁻¹ (commercially elastomer range), we found that a positive α_p lowers oscillation amplitude (Figure 3d). A middle layer with a positive α_p expands upon heating, imposing tensile stress on the adjacent LCEs, opposing their thermal contraction and generating an elastic moment counter to M_T ; the result is reduced amplitude but higher frequency.

Then, we varied three normalized geometric parameters: beam length L/b, active-layer thickness $h_{\rm a}/b$, and passive-layer thickness $h_{\rm p}/b$ around the benchmark configuration (L=2.5 cm, $h_{\rm a}=140~\mu{\rm m}$, $h_{\rm p}=320~\mu{\rm m}$, corresponding to L/b=10, $h_{\rm a}/b=0.056$, and $h_{\rm p}/b=0.128$). Sweeping L/b from 9 to 11 (Figure 3e). θ peaks at the intermediate value L/b=10 (benchmark, $\theta=48.1^{\circ}$) and declines for both shorter and longer oscillators. The nonmonotonicity reflects competition between geometric amplification and damping. Since $\theta \sim \kappa \cdot L$, increasing

L amplifies θ , but also increases surface area, enhancing aerodynamic drag and convective heat loss. The oscillation frequency f follows the expected scaling for a cantilever, $f \propto L^{-2}$.

Varying active-layer thickness $h_{\rm a}/b$ from 0.05 to 0.06 (Figure 3f) yields a nonmonotonic trend in oscillation amplitude θ . A thinner active layer narrows the integration domain (from -h/2 to h/2) and shortens the moment arm (distance from the neutral axis) of $M_{\rm T}$ decreasing the driving moment for oscillation. Yet, a thicker active layer increases bending rigidity (αh^3) and outweighs the effect of increased $M_{\rm T}$. Over this range, oscillation frequency f increases monotonically with $h_{\rm a}/b$. Additionally, increasing passive-layer thickness $h_{\rm p}/b$ from 0.12 to 0.14 (Figure 3g) increases bending rigidity, reducing θ and increasing f.

Lastly, thermal transport governs temperature profiles, the resulting thermal moment, and its interplay with stiffness. Changing thermal conductivity of the active layer (k_a) from 0.54 to 0.66 W m⁻¹ K⁻¹ (Figure 3h) produces a nonmonotonic amplitude with a peak at $k_a = 0.6 \,\mathrm{W \, m^{-1} \, K^{-1}}$ (benchmark). At low k_a , input heat does not penetrate effectively into the interior of the active layer, limiting generated thermal strain. At high k_a , surface heat is rapidly conducted away, flattening the throughthickness temperature gradient and reducing the thermal moment $M_{\rm T}$. The characteristic timescale of heat transfer $\tau_{\rm th}$ can be roughly estimated by $\tau_{\rm th} = h^2/(k/\rho Cp)$, so larger $k_{\rm a}$ shortens τ_{th} , raising the thermal-limited frequency $1/\tau_{th}$. Varying thermal conductivity of the passive layer $k_{\rm p}$ (Figure 3i) also yields a nonmonotonic amplitude. When $k_p < k_a$ [$k_p = 0.54$ and $k_a = 0.6 \text{ W m}^{-1} \text{ K}^{-1}$], the passive layer impedes the heat conduction from the active layer, causing heat accumulation near the active/passive interface and flattening the temperature gradient across the active layer, which weakens thermal moment. When $k_p > k_a$, the passive layer acts as a heat sink that

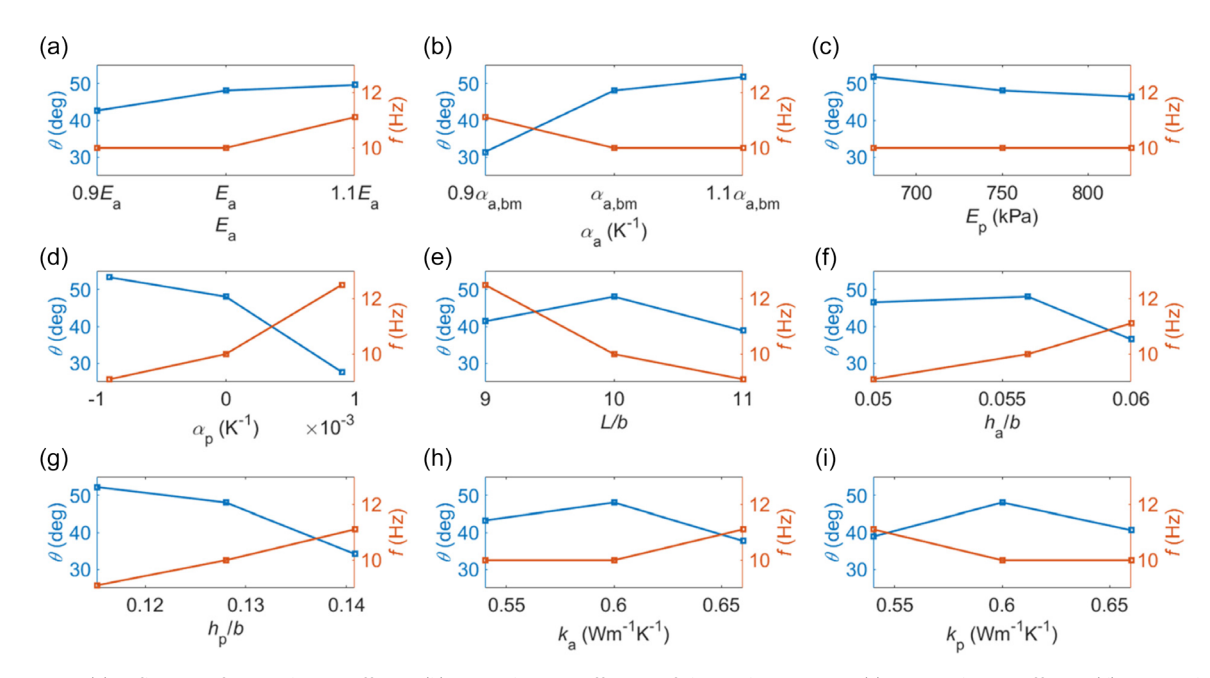


FIGURE 3 I (a) Influence of active-layer stiffness, (b) active-layer coefficient of thermal expansion, (c) passive-layer stiffness, (d) passive-layer coefficient of thermal expansion, (e) length, (f) active-layer thickness, (g) passive-layer thickness, (h) active-layer thermal conductivity, and (i) passive-layer thermal conductivity.

6 of 7 Advanced Robotics Research, 2025

draws heat away from the active layer, lowering its overall temperature and thermal strains, which results in a smaller amplitude.

4 | Conclusion

In this work, we developed a coupled photothermomechanical simulation framework to investigate the dynamics of photothermal self-excited composite oscillators and elucidate the mechanism sustaining oscillation. We establish the criteria and conditions for the onset of self-excited oscillation across various material properties and operating conditions. Although our model system uses photothermal LCE, the numerical framework can readily extend to other autonomous systems with different actuator designs and materials (Supplemental Note 5). The insights gained from this study establish a clear design roadmap for optimizing the performance of photothermal self-excited oscillators and more autonomous actuator and robotic systems.

Acknowledgements

This work used computational and storage services associated with the Hoffman2 Cluster which is operated by the UCLA Office of Advanced Research Computing's Research Technology Group. The authors acknowledge the support from American Chemical Society for award 66747-ND7, Johnson & Johnson for award 20231448, Inventor Fellow award 12072, NIH for award R01DK132319, the Moore Foundation Award 12072, Semiconductor Research Corporation for award 2023-JU3136, and the Office of Naval Research (ONR) for awards N000142412187 and N000142212595.

Conflicts of Interest

The authors declare no conflicts of interest.

Data Availability Statement

The data that support the findings of this study are available from the corresponding author upon reasonable request.

References

- 1. Z.-X. Liu, Y.-J. Qian, X.-D. Yang, and W. Zhang, Aerospace Science and Technology 118 (2021): 107015.
- 2. S. Asakura and A. Ishihara, Sensors and Actuators A: Physical 90 (2001): 111.
- 3. M. Perez, S. Boisseau, P. Gasnier, J. Willemin, and J.-L. Reboud, *Smart Materials and Structures* 24 (2015): 035004.
- 4. Z. Liu a)Y. Zhao, P. Shi, C. Chen, Y. Alsaid, Y. Yan, and X. He, *Nature Materials* 24 (2025): 116.
- 5. P. Shi, Y. Zhao, Z. Liu, and X. He, Journal of Composite Materials 57 (2022): 633.
- 6. Y. Zhao, C. Xuan, X. Qian, et al., Science Robotics 4 (2019): eaax7112.
- 7. Y. Zhao, Q. Li, Z. Liu, et al., Science Robotics 8 (2023): eadf4753.
- 8. M. Hua, C. Kim, Y. Du, D. Wu, R. Bai, and X. He, Matter 4 (2021): 1029.
- 9. F. Gan, Q. Cheng, and K. Li, Journal of Sound and Vibration 526 (2022): 116820.
- 10. X. Fang, Y. Chen, T. Ma, et al., International Journal of Mechanical Sciences 299 (2025): 110424.

- 11. X. Fang, J. Lou, J. Wang, K.-C. Chuang, H. M. Wu, and Z. L. Huang, *International Journal of Mechanical Sciences* 271 (2024): 109124.
- 12. K. Li and S. Cai, Journal of Applied Mechanics 83 (2016): 031009.
- 13. O. Cheng, X. Liang, and K. Li, Nonlinear Dynamics 103 (2021): 2437.
- 14. T. Sun, K. Li, Y. Dai, and J. Zhao, *International Journal of Mechanical Sciences* 227 (2022): 107439.
- 15. X. Liang, Z. Chen, L. Zhu, and K. Li, Mechanical Systems and Signal Processing 163 (2022): 108140.
- 16. C. Bai, J. Kang, and Y. Q. Wang, *International Journal of Mechanical Sciences* 266 (2024): 108911.
- 17. K. Li, Y. Qiu, Y. Dai, and Y. Yu, International Journal of Mechanical Sciences 263 (2024): 108794.
- 18. P. Xu, J. Jin, and K. Li, International Journal of Mechanical Sciences 208 (2021): 106686.
- 19. P. Xu, X. Sun, Y. Dai, and K. Li, International Journal of Mechanical Sciences 266 (2024): 108922.
- 20. D. Ge, J. Jin, Y. Dai, P. Xu, and K. Li, Polymers 14 (2022): 2770.
- 21. C. Xuan, Y. Zhou, Y. Zhao, X. He, and L. Jin, *Physical Review Applied* 17 (2022): 014007.
- 22. X. Qian, Y. Zhao, Y. Alsaid, et al., Nature Nanotechnology 14 (2019): 1048.
- 23. Y.-J. Qian, L.-E. Zuo, Z.-X. Liu, X.-D. Yang, and L. Xu, *AIAA Journal* 61 (2023): 497.

Supporting Information

Additional supporting information can be found online in the Supporting Information section. Supporting Fig. S1: Quantitative comparison of oscillation angle (a), frequency (b), and kinetic power density (c) between simulations (blue bars) and experiments (pink bars). **Supporting Fig. S2**: Effect of geometric nonlinearity on simulated oscillator morphology. a. Finite deformation (geometric nonlinearity on). b. Small-strain model (geometric nonlinearity off). Neglecting geometric nonlinearity produces spurious beam elongation under thermal contraction. Color bar: temperature field of the oscillator. Supporting Fig. S3: Quasi-static light tracking when structural inertia is neglected. Red and blue curves correspond to tilt angles of 0° and 10°, respectively. Insets show the corresponding equilibrium beam morphologies: without inertia, the beam settles into a light-aligned equilibrium rather than sustained oscillation. Supporting Fig. S4: Effect of laser spot size H_L on self-sustained oscillation. Time history of oscillation amplitude θ for $H_L = 35$ mm (red) and 4 mm (blue) at identical power density. Insets show the beam temperature fields at t=4.2 s. Supporting Fig. S5: State diagrams in the $(S, H_{\rm L})$ plane (a; L = 2.5 cm) and the (H_L , L) plane (b; S = 2,000 mW·cm⁻²) that delineate the oscillatory and non-oscillatory regimes. Supporting Fig. S6: Effect of convective cooling on oscillation and temperature. a. Oscillation angle θ for $\lambda = 35$ (blue), 45 (orange), and 55 (yellow) W·m⁻²·K⁻¹. Inset shows the oscillation from t = 15 s to 16 s. b. Temperature evolution at point (0.2L, 0) of oscillators with $\lambda = 35 \sim 55 \,\mathrm{W \cdot m^{-2} \cdot K^{-1}}$. Supporting Fig. S7: Effect of tile angle on oscillation amplitude θ . Supporting Fig. S8: Eu-Pdimi-PDMS-based bilayer oscillator driven by a static temperature gradient. a. Simulation setup and snapshots of beam morphology and temperature. b. Time evolution of the oscillation angle, showing growth to a steady selfsustained oscillation. Supporting Table S1: Simulation parameters for the Eu-Pdimi-PDMS-based bilayer oscillator.

Advanced Robotics Research, 2025 7 of 7